Check for updates

View Article Online
View Journal

Chemical
Science

Accepted Manuscript

This article can be cited before page numbers have been issued, to do this please use: S. Zhang, Y. Ma, C. Yu, Z. Huang, R. Zhan, Y. Wang, X. Xie and N. Zhang, *Chem. Sci.*, 2025, DOI: 10.1039/D4SC07856J.

ROYAL SOCIETY
OF **CHEMISTRY**

rsc.li/chemical-science

View Article Online
DOI: 10.1039/D4SC07856J

ARTICLE

Modulating PCET Process *via* Optimizing Local Microenvironment of CdS@NiV-LDH Heterojunction for CO_2 Reduction to Tunable Green Syngas Photosynthesis

Received 00th January 20xx,
Accepted 00th January 20xx

DOI: 10.1039/x0xx00000x

Senlin Zhang,[a‡] Yuheng Ma,[a‡] Changqiang Yu,[a] Zhaohui Huang,[a] Ruoning Zhan,[a] Yingxinjie Wang,[a] Xiuqiang Xie[*a] and Nan Zhang[*a]

Photoconversion of CO_2 and H_2O into syngas (CO + H_2) for the Fischer-Tropsch reaction is considered a feasible plan to address global energy requirements in times of global warming. However, the production of syngas with high activity and adjustable proportion is challenging mainly because of the less efficient multi-step proton-coupled electron transfer (PCET) process owing to the unfavorable local microenvironment of photocatalysts. Herein, an S-scheme CdS@NiV-LDH (HNV) heterojunction is constructed through mild wet-chemistry methods, and the NiV-LDH nanosheets are uniformly grown *in-situ* on the surface of the hollow cubic CdS (HCC). The as-prepared three-dimensional hierarchical architecture of the HNV photocatalyst exhibits a controllable CO/H_2 ratio ranging from 0.2 to 1, and the CO and H_2 production rate of the optimal HNV-4 heterojunction can reach 1163.8 μmol/g/h and 1334.6 μmol/g/h, respectively. X-ray photoelectron spectroscopy, electron spin spectroscopy, and photo-deposition platinum metal test show that the photogenerated charge carriers in HNV follow an S-scheme charge transfer mechanism. This significantly improves the spatial separation of the photogenerated electron-hole pairs *via* the built-in electric field that modifies the electric field microenvironment of the HNV photocatalyst to accelerate the photoreduction process. Meanwhile, the NiV-LDH nanosheets on the external surface act as a CO_2 enricher and H_2O moderator that adjusts the reaction microenvironment to speed up the PCET process by increasing the local CO_2 concentration and facilitating *COOH intermediate generation in the HNV heterojunction. This work opens a new horizon for exploring novel heterogeneous photocatalysts toward enhanced visible-light-driven CO_2 conversion to tunable green syngas.

1. Introduction

In the last century, the increasing demand for energy in daily life, extensive reliance on traditional fossil fuels, and ongoing deforestation have led to a continuing increase in the atmospheric carbon dioxide (CO_2) level.[1-3] Inspired by the natural photosynthesis process, the researchers have found that the solar energy-mediated photocatalytic pathways hold promising and durable solutions to achieve the goals of "Carbon Neutrality" by efficiently converting CO_2 into high-value-added chemicals and fuels.[4-6] There are many varieties of CO_2 photoreduction products (such as CO, HCOOH, CH_3OH, CH_4, C_2, C_{2+}, etc.), of which carbon monoxide (CO) has attracted special attention as one of the most valuable raw materials for Fischer-Tropsch synthesis (FTS) to produce hydrocarbon liquid fuels, which is expected to replace the petroleum-based processes.[7,8] In industrial processes, adjusting the ratio of CO and hydrogen (H_2) in the syngas is essential to meet the specific chemical requirements due to that the syngas (i.e., a mixture of CO and H_2) is a versatile feedstock for FTS synthesis.[9] For instance, dimethyl ether, methanol, and syngas fermentation can be produced with ratios of CO/H_2 at 0.3, 0.5, and 1, respectively. The syngas are predominantly produced in harsh synthetic conditions and proportionally uncontrollable, which is traditionally obtained by coal gasification, natural gas reforming, or water-gas reforming reactions.[10] Photocatalytic CO_2 reduction to syngas can be achieved under room temperature (ca. 25 °C) and normal pressure (1 atm) using solar energy alone.[11] While, the efficiency of current photocatalytic CO_2-to-syngas reduction systems is still unsatisfactory, mainly due to the easy recombination of charge carriers, insufficient activation of CO_2 molecules, and hydrogenation competition reaction.[12,13] These factors restrict the reaction kinetics seriously and lead to unfavorable syngas ratios.[14] Therefore, developing photocatalytic materials empowering efficient charge separation, outstanding CO_2 activation, and wide adjustable syngas ratio is considered an available strategy to improve CO_2 reduction efficiency, but remains challenging.

Among the semiconductor materials reported for CO_2 photoreduction, cadmium sulfide (CdS) has been a focus of research due to its narrow band gap (ca. 2.4 eV), adequate negative conduction band potential for the reduction of CO_2 to CO, and nanosize-tunable electronic structure.[15,16] Moreover, the hollow-structured photocatalysts with large surface areas and abundant active sites show distinct advantages for solar energy conversion reactions.[17] For instance, the thin shells of the hollow structure could reduce the distance for the transfer

---

[a] College of Materials Science and Engineering, Hunan University, Changsha 410082, China. E-mail: xiuqiang_xie@hnu.edu.cn; nanzhang@hnu.edu.cn

† Electronic Supplementary Information (ESI) available: characterization details and additional results. See DOI: 10.1039/x0xx00000x

‡ Senlin Zhang and Yuheng Ma contributed equally to this work.

of photogenerated charge carriers, and the light scattering effect can be enhanced, which would lead to enhanced light absorption capability.[18-20] However, the photocatalytic efficiency of CO_2 to syngas over conventional CdS-based catalysts is still low, accompanied by the inapplicable syngas ratio with an over-higher share of H_2 compared to CO.[21,22] This is mainly caused by the inherent microenvironment of CdS with a weak electric field microenvironment leading to inefficient photogenerated carrier separation capability,[23] and an unsuitable reaction microenvironment leading to inadequate CO_2 adsorption and activation and thus unsatisfactory product distribution.[24,25] Meanwhile, a class material of layered double hydroxides (LDHs) with alkalinity has attracted great attention in the field of photocatalytic CO_2 reduction due to their favorable CO_2 adsorption capability.[26-28] Tanaka et al.[29] for the first time demonstrated the photocatalytic conversion of CO_2 (dissolved in water) into CO and O_2 on various M^{2+}-M^{3+} LDHs. More recently, the NiAl-LDH was developed for photocatalytic CO_2 reduction, with a CO evolution rate of 1.01 μmol/g/h, and the selectivity towards CO almost attaining 59.8%.[30] Although native LDHs have exhibited great potential for photocatalytic reduction of CO_2 to CO, the drawbacks, especially the sacrificing catalytic active sites on LDHs due to aggregation effect during the synthesis process still limit the conversion efficiency.[31]

Recent research has revealed that the overall CO_2 photoreduction with H_2O is a proton-coupled electron transfer (PCET)-involved complex surface-interface reaction process, which is controlled by the intricate microenvironment provided by unique photocatalysts.[32,33] It is worth noting that the thermodynamic and kinetic processes of proton (H^+) produced from H_2O molecules in the presence of both CO_2 and H_2O are sophisticated.[24,25,31] Being quite different from the reaction system that aims to realize efficient CO_2 reduction and simultaneously minimize the protons coupling to H_2 production,[21,34] the reduction of CO_2 and H_2O to green syngas needs to "balance" the CO_2 reduction and protons reduction processes. Under the situation, it is essential to unveil whether the protons prefer to bind with $CO_2^{\bullet-}$ to generate *COOH intermediate for efficient generation of the product CO through the PCET process or rapidly coupled to each other to produce H_2. More importantly, revealing how the microenvironment engineering affects the above processes is of significant importance to obtain green syngas with tunable CO/H_2 ratio from photoreduction of CO_2 and H_2O. However, the research in this regard is still scarce.[35]

Herein, an S-scheme heterojunction CdS@NiV-LDH (HNV) photocatalyst is constructed by mild wet-chemistry methods and applied to reduce CO_2 for syngas synthesis. The HNV heterojunctions are adjusted by varying the content of NiV-LDH to achieve the photocatalytic CO_2 reduction into syngas with adjustable ratios in the wide range of 0.2~1. Among them, the total generation rate of green syngas from photoreduction of CO_2 by the optimal HNV is 2498.4 μmol/g/h. Various complementary characterizations collectively confirm that the special three-dimensional (3D) hierarchical architecture of optimal catalyst with hollow CdS nanocube inner cavity and rough external surface modified by NiV-LDH nanosheets has efficient visible light absorption, rapid charge separation and migration, and favorable localized CO_2 concentration and mass transfer efficiency. Based on the above, this well-designed photocatalyst with an optimized electric field microenvironment and reaction microenvironment can significantly increase syngas yield as well as achieve tunable CO/H_2 ratios by accelerating the PCET process to facilitate the formation of *COOH intermediate. The special 3D hierarchical architecture may shed light on the rational design of advanced materials and reaction systems for photocatalytic CO_2 reduction to produce green syngas.

2. Experimental section

2.1 Materials

All materials were of analytical grade and used as received without further purification, and detailed information is provided in the ESI.†

2.2 Preparation of photocatalysts

Experimental procedures for preparing different photocatalysts in this study are provided in the ESI.†

2.3 Characterization

Specific details are provided in the ESI.†

2.4 Photoelectrochemical measurements

Photoelectrochemical measurements were carried out in an electrochemical workstation (CHI 660E, Shanghai Chenhua, China) with a conventional three-electrode system. Specific operational information is provided in the ESI.†

2.5 Measurement of photocatalytic CO_2 Reduction

Reactions of photocatalytic CO_2 reduction were conducted in a custom-made reactor with a 300 W Xe lamp with a 420 nm cutoff filter (PLS-SXE 300E, Beijing Perfect Light Co. Ltd.) and analyzed by gas chromatograph (Shimadzu GC-2014, 5 A molecular sieve column). Specific operational information is provided in the ESI.†

2.6 Calculation of Apparent Quantum Yield of Syngas Production

Monochromatic lights with wavelengths of 365, 450, 500, and 605 nm are used for irradiation for 1 hour. Specific operational information is provided in the ESI.†

2.7 Experiment of *in-situ* photodeposition

$H_2PtCl_6\cdot H_2O$ solution containing 3 wt.% Pt relative to the photocatalyst was added dropwise to the suspension of the HNV-4 photocatalyst. After degassing and backfilling the mixture with N_2, the suspension was then irradiated for 1 hour with a 300 W Xe lamp (λ > 420 nm). Specific operational information is provided in the ESI.†

3. Results and discussion

The fabrication process of the CdS@NiV-LDH (HNV) composite is displayed in Fig. 1a. Cadmium Prussian blue analog (Cd PBA)

View Article Online
DOI: 10.1039/D4SC07856J

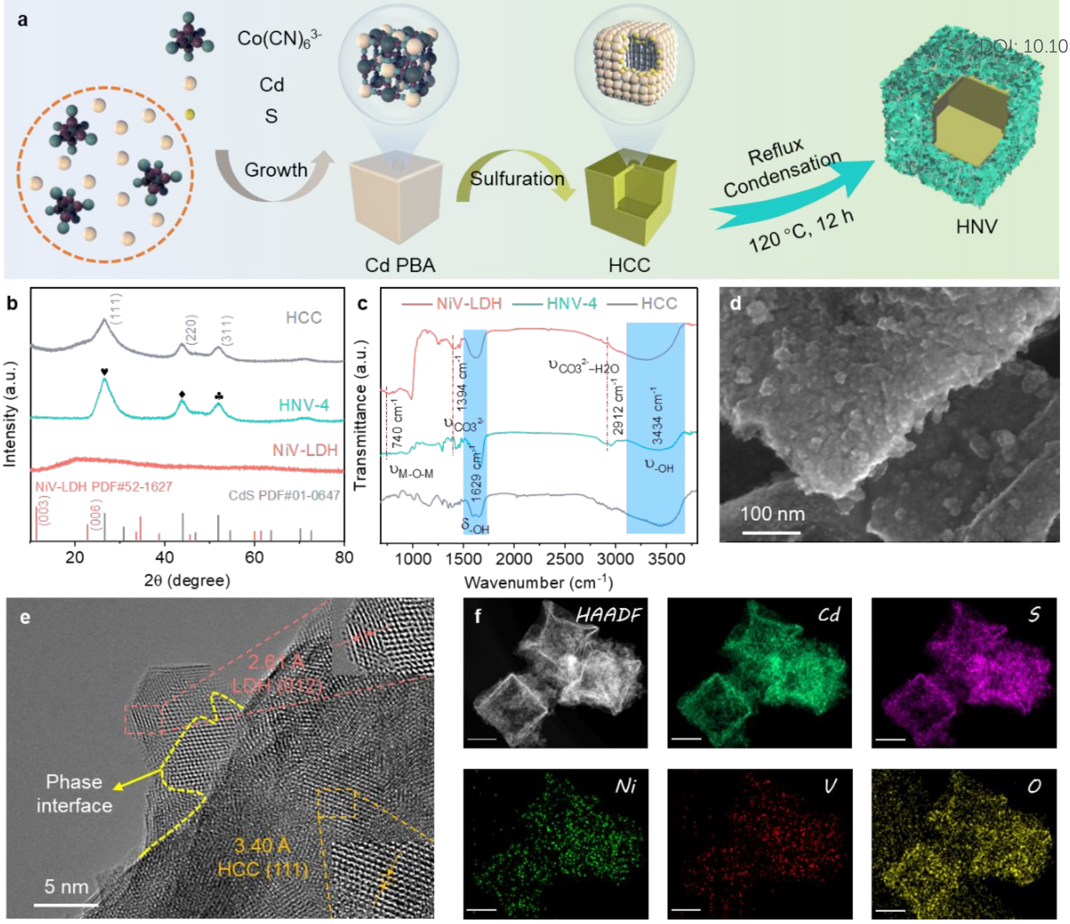

Fig. 1 (a) Schematic flowchart for synthesis of HNV composite. (b) XRD and (c) FT-IR patterns of HCC, NiV-LDH, and HNV-4. (d) SEM and (e) HR-TEM images of HNV-4. (f) HAADF-STEM and corresponding EDS element mapping images of HNV-4 (scale bar: 200 nm).

precursor is synthesized by a facile solution-based ion exchange/precipitation method (the ion exchange of K$^+$ to Cd$^+$). Then, Cd PBA is converted into hollow cadmium sulfide cubes (HCC) through a sulfidation process using TAA and Na_2S as sulfur sources.[36] Finally, NiV-layered double hydroxide (NiV-LDH) nanosheets (NSs) are *in-situ* growing on the surface of HCC through the one-pot reflux method. The as-prepared composite samples with different loadings of NiV-LDH NSs are named HNV-X (X = 1, 2, 3, 4, 5 corresponding to the increased content of NiV-LDH) (Table S1†). The crystalline structure of the samples is investigated by X-ray diffraction (XRD), which is displayed in Fig. 1b and Fig. S1†. For the pure HCC, the distinct diffraction peaks at 26.4°, 43.8°, and 51.8° are indexed to the (111), (220), and (311) crystal planes of cubic hawleyite cadmium sulfide (JCPDS No. 01-0647), respectively.[18] While, the XRD pattern of NiV-LDH exhibits a wide diffraction peak appears at ca. 20.3°, corresponding to the (006) crystal plane of NiV-LDH (JCPDS No. 52-1627), and the peak for NiV-LDH NSs is shifted to a lower angle ca. 2.5° compared to the standard card, which might be ascribed to the enlarged interlayer space of (006) plane or the formation of monolayer NiV-LDH NSs.[37] In addition, the diffraction peak at 11.6° corresponds to the (003) crystal plane of NiV-LDH cannot be observed, which belongs to the characteristic peak of layered structure for LDHs, indicating that the as-prepared NiV-LDH does not have an obvious multilayer structure.[38] The diffraction pattern of NiV-LDH cannot be observed in HNV composites (Fig. S1†). To understand this phenomenon, the accurate content of NiV-LDH in the composite is determined (Table S2†). Taking HNV-4 as an example, the NiV-LDH loading content is 48.0 wt.%, which value should reach the XRD detectability. According to the above analysis, the absence of NiV-LDH XRD pattern in the HNV composites should be ascribed to the large interlayer space and monolayer structure of NiV-LDH as well as the uniform distribution of NiV-LDH nanosheets on the surface of the HCC. There are no obvious changes in characteristic peaks of HCC for the composite samples, indicating that the crystal structure of cubic hawleyite cadmium sulfide (CdS) does not change in the formation process of HNV with the introduction of NiV-LDH.[39] Fourier transform infrared (FT-IR) spectroscopy is applied to investigate the chemical environment of samples. Fig. 1c displays the FT-IR spectra of HCC, NiV-LDH, and HNV-4, all of which exhibit broad and strong absorption peaks at 3434 cm^{-1} and 1629 cm^{-1} indicating the presence of stretching and bending modes of hydroxyl (-OH) groups, arising from adsorbed water molecules and metal-hydroxyl groups.[40] Interlayer anions CO_3^{2-} and CO_3^{2-}-H_2O of NiV-LDH are confirmed through vibration peaks at 1394 cm^{-1} and 2912 cm^{-1}, respectively, confirming the presence of hydrogen-bonded water molecules with carbonate anions in the interlayer of

View Article Online
DOI: 10.1039/D4SC07856J

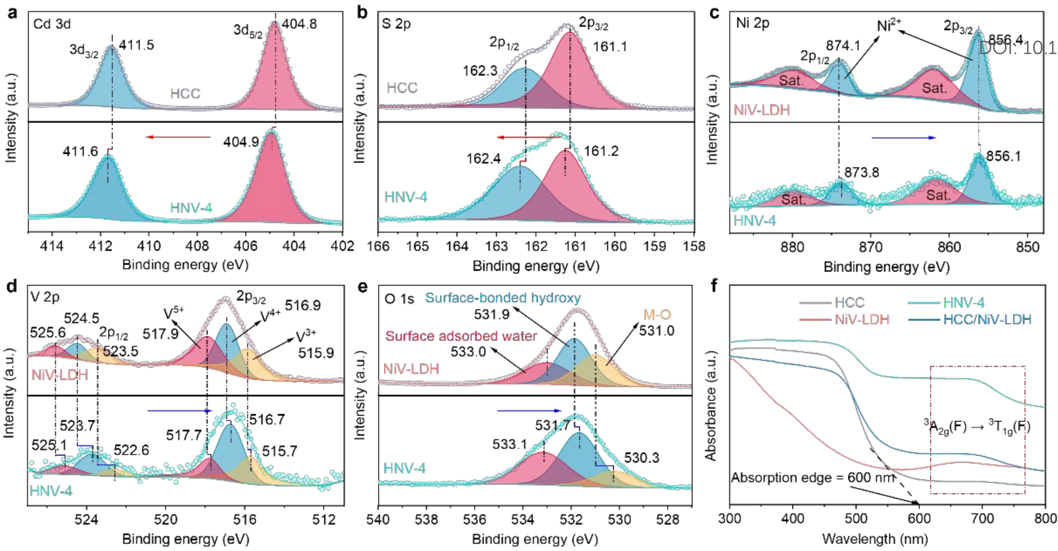

Fig. 2 High-resolution XPS spectra of (a) Cd 3d and (b) S 2p of HCC and HNV-4 and (c) Ni 2p, (d) V 2p and (e) O 1s of NiV-LDH and HNV-4, respectively. (f) UV-vis diffuse reflectance spectra (DRS) of HCC, NiV-LDH, HNV-4, and HCC/NiV-LDH.

NiV-LDH.[28] The absorption peak at 740 cm^{-1} (less than 800 cm^{-1}) is ascribed to the stretching vibrations of metal-oxygen bonds present in NiV-LDH.[41] In comparison with HCC and NiV-LDH, all FT-IR characteristic peaks of the HNV-4 composite are consistent with that of the pure component, indicating that the NiV-LDHs are successfully combined with HCC.

The morphology and microstructure of the as-prepared samples are investigated by scanning electron microscopy (SEM) and high-resolution transmission electron microscopy (HR-TEM). After the sulfidation reaction of the Cd PBA template, the HCC is formed through a mechanism similar to the nanoscale Kirkendall effect,[42] and the surface of the HCC is smooth and uniformly dispersed (Fig. S2a†). Moreover, there are slight collapse on the geometric surfaces of HCC, which is caused by the inward shrinkage of the nano-cubic nuclei during the sulfidation process.[18] It can be seen from Fig. S2b† that the pure NiV-LDHs demonstrate smooth nanosheet morphology with the size of 100~200 nm that agglomerate with each other. Compared to the single components, the surface of HNV-4 becomes rough (Fig. S2c†) and the NiV-LDH NSs are uniformly distributed over the surface of the CdS nanocubes (Fig. 1d), which prevents the nanosheet from aggregating and provides more surface areas and active sites for the rapid transport and migration of matters. As seen in the HR-TEM images (Fig. 1e and Fig. S3†), the lattice fringes of 3.40 Å and 2.61 Å are determined, which correspond to the (111) crystal facet of cubic CdS and (012) crystal facet of NiV-LDH, respectively. Moreover, there is a clear interface intersection region between the two components, and the formation of tightly contact interfaces plays a significant role in space separation and migration of electron-hole pairs. In addition, the uniform distribution of Cd, S, Ni, V, and O elements measured by the energy dispersive spectrometer (EDS) further demonstrates the successful preparation of the three-dimensional (3D) hollow hierarchical CdS@NiV-LDH composite (Fig. 1f).

The surface elemental composition and chemical states of the samples are analyzed by X-ray photoelectron spectroscopy (XPS). Characteristic peaks of Cd, S, Ni, V, and O elements are detected in the HNV-4 composite (Fig. S4†), which is consistent with the high-angle annular dark-field scanning transmission electron microscope (HAADF-STEM) element mapping results (Fig. 1f). As revealed in Fig. 2a, the high-resolution Cd 3d spectrum of the HNV-4 composite with peaks situated at 404.9 (Cd 3d$_{5/2}$) and 411.6 eV (Cd 3d$_{3/2}$) is attributed to Cd^{2+} species. The high-resolution S 2p spectrum of the HNV-4 composite exhibits two featured peaks at 161.2 (S 2p$_{3/2}$) and 162.4 eV (S 2p$_{1/2}$), ascribed to the S^{2-} species (Fig. 2b). Notably, compared with pristine HCC, the Cd 3d and S 2p peaks of the HNV-4 composite are shifted to higher binding energy resulting from the decreasing electron cloud density of HCC in the HNV-4 composite.[22] The high-resolution Ni 2p spectrum of HNV-4 shows two distinct peaks at 856.1 and 873.8 eV that correspond to Ni 2p$_{3/2}$ and Ni 2p$_{1/2}$, respectively, and two satellite peaks are also observed at 861.7 and 879.4 eV, indicating the native characteristic of Ni^{2+} spectra (Fig. 2c). As shown in Fig. 2d, the V 2p spectrum displays the presence of V 2p$_{3/2}$ and V 2p$_{1/2}$ peaks due to the spinning *p* orbital splitting. The high-resolution V 2p$_{3/2}$ of HNV-4 can be deconvoluted into three binding energy components, corresponding to V^{3+} (515.7 eV), V^{4+} (516.7 eV), and V^{5+} (517.7 eV). The high-resolution V 2p$_{1/2}$ of HNV-4 also can be deconvoluted into three binding energy components, corresponding to V^{3+} (522.6 eV), V^{4+} (523.7 eV), and V^{5+} (525.1 eV), implying that portion of V^{3+} was oxidized to V^{4+} and V^{5+} during the oil bath process.[40] The high-resolution O 1s spectrum of HNV-4 can be deconvoluted into three distinct peaks located at 530.3, 531.7, and 533.1 eV that correspond to metal-oxygen (M-O, where M represents Ni or V) bonds, surface-bonded hydroxyl groups (-OH), and surface-adsorbed water molecules, respectively (Fig. 2e).[43] Different from the peak values shift of Cd 3d and S 2p, the core horizontal spectra of Ni 2p, V 2p, and O 1s for the HNV-4 composite shift to the lower deconvolution peak values

View Article Online
DOI: 10.1039/D4SC07856J

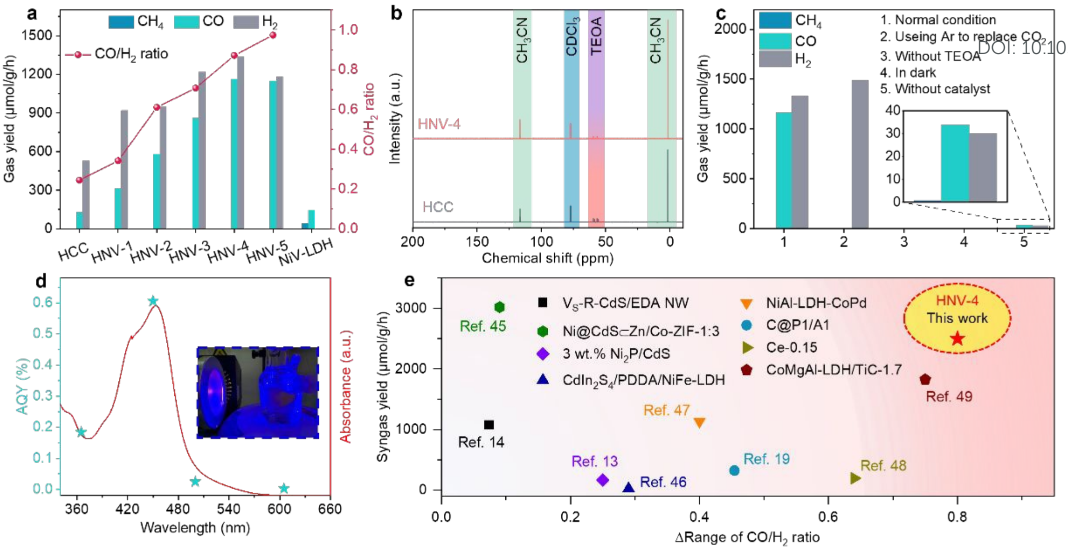

Fig. 3 (a) Product yield over HCC, NiV-LDH, and HNV-X (X = 1, 2, 3, 4, 5). (b) ^{13}C NMR spectra of liquid phase products after photocatalytic CO_2 reduction of HCC and HNV-4. (c) CO_2 photoreduction of control experiment under different conditions. (d) AQY results of HNV-4 along with the absorption spectrum of the $[Ru(bpy)_3]Cl_2{\cdot}6H_2O$ photosensitizer. The inset is the corresponding photograph of the experiment setup. (e) Tunable range of CO/H_2 ratios and syngas yield of photocatalytic CO_2 reduction over HNV-4 in comparison with some typical CdS-based and LDH-based photocatalysts.

compared with pure NiV-LDH resulting from the increasing electron cloud density of NiV-LDH in the HNV-4, implying the charge accumulation on the surface of NiV-LDH in the composite. Compared to pure HCC and NiV-LDH, the relative shift direction of the main peaks for corresponding components in the HNV-4 composite suggests a strong interfacial interaction between HCC and NiV-LDH. In other words, the CdS@NiV-LDH heterostructure has been successfully prepared.

Based on the strong interaction between the HCC and NiV-LDH, the light absorption capability of the HNV heterostructure exhibits distinct synergistic effects. As shown in Fig. 2f, HCC displays an obvious visible light response with an absorption edge extended to 600 nm, which is attributed to the intrinsic bandgap photoexcitation of CdS. Pristine NiV-LDH possesses a wider light response range but lower intensity, with apparent light absorption across the range of wavelengths measured (200~800 nm). Resulting from the spin-orbit coupling, the absorption band at 645-710 nm of NiV-LDH corresponds to the $^3A_{2g}(F) \rightarrow {}^3T_{1g}(F)$ transition of Ni^{2+}.[38] According to the Tauc plots (Fig. S5†), the corresponding bandgap (E_g) of HCC and NiV-LDH are determined to be 2.40 and 1.73 eV, respectively. As for HNV heterostructures, both absorptions corresponding to HCC and NiV-LDH can be observed (Fig. S6†), indicating the successful combination of HCC and NiV-LDH. Notably, the all of heterostructures show a stronger absorption at 600~800 nm, and HNV-4 behaves with stronger absorption than bare HCC and NiV-LDH. In addition, the HCC/NiV-LDH composite prepared by mechanical milling exhibits significantly lower light-harvesting capacity than HNV-4, manifesting a more favorable synergistic effect in the CdS@NiV-LDH heterostructure that is constructed by an *in-situ* growth strategy.

Subsequently, the CO_2 photocatalytic reduction (CO_2PR) performance of the samples is studied under visible light irradiation (λ > 420 nm) in a mixture of acetonitrile (CH_3CN) and water with triethanolamine (TEOA) as a sacrificial agent of photogenerated holes and $[Ru(bpy)_3]Cl_2{\cdot}6H_2O$ as a photosensitizer. The gaseous and liquid products are analyzed by gas chromatography and nuclear magnetic resonance (NMR), respectively. As depicted in Fig. 3a, the CH_4 and CO production rates over the pure NiV-LDH are 41.2 μmol/g/h and 144.5 μmol/g/h, respectively, and no other gas product such as H_2 is observed. The products of CO and H_2 are mainly observed for HCC and HNV-X (X = 1, 2, 3, 4, 5), and the yield of CH_4 is all less than 2 μmol/g/h. With the increasing of NiV-LDH NSs loading, the generating rates of CO and H_2 gradually increase for HNV-X heterostructures, accompanied by an increase in the rate of syngas production. Thereinto, the optimal CO, H_2, and syngas production rates are observed over HNV-4, which are determined to be 1163.8 μmol/g/h, 1334.6 μmol/g/h, and 2498.4 μmol/g/h, respectively. The CO production rate of the optimal HNV-4 sample is approximately 9-fold and 8-fold as high as that of pure HCC and NiV-LDH, respectively. Intriguingly, the ratio of the CO/H_2 product over HNV-X heterojunctions can be tunable from 0.2 to 1, and the tunable syngas is not only an ideal feedstock for the Fischer-Tropsch process but also favors the synthesis of low-carbon olefins (C_2-C_4).[44] Moreover, the liquid products have been detected by the ^{13}C NMR measurement after photocatalytic CO_2 reduction of HCC and HNV-4. The signals in Fig. 3b are attributed to CH_3CN, TEOA, and deuterated chloroform ($CDCl_3$), respectively. No additional peaks appeared in the ^{13}C NMR spectra other than those of the reaction solution and the test reagent, proving that no liquid products are generated in the present reaction system. By comparing the intensity of ^{13}C NMR signals for HCC and HNV-4, it is noticed that the TEOA

View Article Online
DOI: 10.1039/D4SC07856J

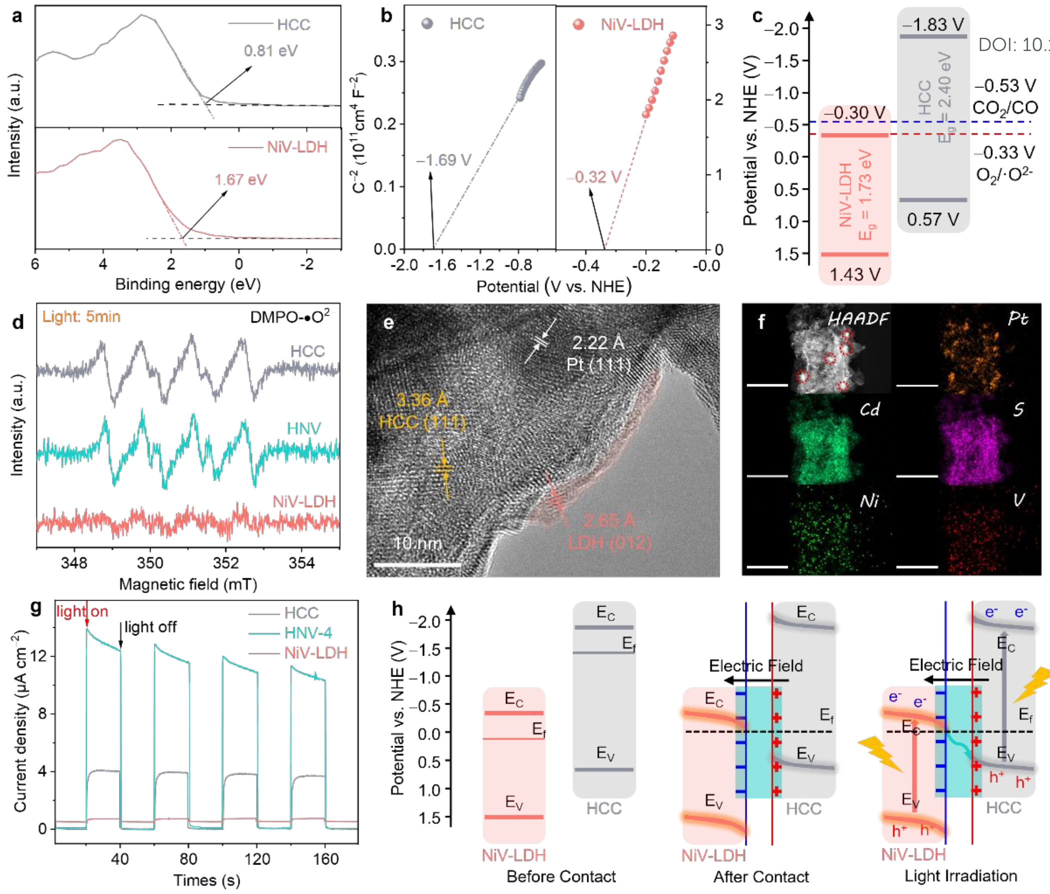

Fig. 4 (a) XPS valence band spectra of HCC and NiV-LDH. (b) Mott-Schottky plots of HCC and NiV-LDH under 1000 Hz. (c) Band structure of HCC and NiV-LDH (*vs.* NHE). (d) ESR spectra of DMPO-•O^{2-} adducts over HCC, NiV LDH, and HNV-4 after irradiation. (e) HR-TEM and (f) HAADF-STEM and corresponding EDS element mapping images of HNV-4@Pt (scale bar: 200 nm). (g) Transient photocurrent responses of HCC, NiV-LDH, and HNV-4. (h) Proposed intrinsic mechanism of S-scheme electron migration pathway for HNV-4 heterojunction.

peak in the HNV-4 is smaller than the corresponding peak intensity in the HCC, which is attributed to the fact that the HNV-4 heterostructure effectively promotes the spatial separation of photogenerated electrons and holes, and more TEOA is consumed by the holes.

In the process of photocatalytic reduction of CO_2, it is necessary to explore the impact of some major experimental conditions on the reduction products.[45] When replacing CO_2 with Ar as the gas source or in the absence of TEOA or light irradiation in the catalytic system, CO cannot be detected, indicating that CO_2, sacrificial agent, and light irradiation are essential for the present catalytic reactions (Fig. 3c, groups 2, 3, 4). Furthermore, only a few amounts of CO and H_2 can be detected without the catalyst, which is because the photosensitizer could act as the molecule catalyst to form homogeneous catalytic systems (Fig. 3c, group 5).[13] Compared with the high yield of the system under normal conditions, the trace amounts of CO and H_2 generated by $[Ru(bpy)_3]Cl_2·6H_2O$ contribute barely to the catalytic performance, suggesting that the obtained green syngas mainly come from the photocatalytic reduction over HNV-4. The variation trend of the apparent quantum yield (AQY) over different incident light wavelengths matches with the absorption spectrum of $[Ru(bpy)_3]Cl_2·6H_2O$ (Fig. 3d), and the highest AQY can be up to 0.606% at a monochromic wavelength of 450 nm (Table S3†). Meanwhile, These results show that our photoreduction CO_2 system is driven by the photoexcitation of $[Ru(bpy)_3]Cl_2·6H_2O$, generating electrons to achieve the reduction process, wherein the HNV-4 composite serves as a medium to accelerate electron transmission to reduce CO_2. Furthermore, in the absence of the presence of $[Ru(bpy)_3]Cl_2·6H_2O$, HNV-4 can reach an AQY of 0.162% at a monochromic wavelength of 365 nm, and the trend of the AQY with incident light wavelength is matching with the UV-vis DRS of HNV-4 (Fig. S7† and Table S3†). As displayed in Fig. 3e and Table S4†, the tunable range of CO/H_2 ratio (Δrange of CO/H_2 ratio) achieves 0.8, which is significantly higher than that of some typical CdS-based and LDH-based photocatalysts, while maintaining a high syngas yield.[15,16,22,46-50] Besides, the HNV-4 sample after the photoreduction reaction has been analyzed. It can be seen from the XPS spectra (Fig. S8†) that the chemical composition and the binding energy values of the elements for the used HNV-4 remain unchanged, indicating its favorable photostability.

To reveal the underlying mechanism of the photocatalytic reduction progress for the prepared catalysts, various complementary characterizations are conducted. The valence band (VB) of the samples is evaluated from the corresponding valence band (VB) XPS spectrum (see in Fig. 4a), where the corresponding $E_{VB,\,XPS}$ of HCC and NiV-LDH are measured to be

View Article Online
DOI: 10.1039/D4SC07856J

0.81 and 1.67 eV, respectively. Then, the E_{VB} of the corresponding standard hydrogen electron ($E_{VB,\ NHE}$) can be calculated according to the following formula: $E_{VB,\ NHE} = \phi + E_{VB,\ XPS} - 4.44$, where ϕ is the work function of the instrument (4.20 eV). Thus, the $E_{VB,\ NHE}$ of HCC, and NiV-LDH are calculated to be 0.57 and 1.43 V, respectively. Following the equation of $E_{FB,\ NHE} = E_{Ag/AgCl} + E^{\varnothing}_{Ag/AgCl}$, where $E^{\varnothing}_{Ag/AgCl}$ is 0.198 V, the flat band (FB) potentials of HCC and NiV-LDH are calculated to be –0.32 and –1.69 V *vs*. NHE by Mott-Schottky measurement, respectively (Fig. 4b). The positive slope of the fitting curve indicates that the HCC and NiV-LDH are n-type semiconductors, and the conductive band value (E_{CB}) for n-type semiconductors is usually more negative than the E_{FB} of approximately 0.1~0.3 V.[30] Moreover, according to the values of E_g and $E_{VB,\ NHE}$, the values of the $E_{CB,\ NHE}$ for HCC and NiV-LDH are –1.83 and –0.30 V, respectively.[21] As shown in Fig. 4c, if the photoinduced charge carriers are transported through a conventional type-Ⅱ heterojunction route, the photogenerated electrons of HCC would migrate to the CB of NiV-LDH to reduce CO_2 or protons (H^+),[51] while the CB potential of NiV-LDH is lower than the reduction potential of H^+/H_2 (–0.41 V *vs*. NHE) and CO_2/CO (–0.53 V *vs*. NHE), indicating that the component of NiV-LDH cannot produce syngas from thermodynamics. Moreover, NiV-LDH can catalyze the production of CH_4 (CO_2/CH_4, –0.24 V *vs*. NHE), in agreement with the results of Fig. 3a, and yet the products of HNV-X composites contain barely CH_4. Therefore, the type-Ⅱ heterojunction mechanism is not suitable for the HNV-4 heterostructure.

The realistic charge transfer mechanism of HNV heterostructure is validated through the electron spin resonance (ESR) measurement. In detail, 5, 5-dimethyl-1-pyrroline-*N*-oxide (DMPO) is used as a spin-trapping reagent in the HNV-4 heterostructure system, and the $\bullet O^{2-}$ is generated by the electron injection to dissolved O_2 in methanol, and the transient radical will transform to DMPO-$\bullet O^{2-}$ adduct which is a stable radical that is suitable for ESR detection. As depicted in Fig. 4d, the six characteristic peaks assigned to DMPO-$\bullet O^{2-}$ adducts are presented for HCC and HNV-4 after 5 minutes of visible light irradiation, while no signal is observed for the pure NiV-LDH, suggesting that photogenerated electrons used in the reduction reaction are mainly accumulated on the CB of HCC, not on NiV-LDH whose E_{CB} is not negative enough to produce $O_2/\bullet O^{2-}$ (–0.33 V *vs*. NHE).[52]

To further prove the successful matching of S-scheme heterojunction, we then ascertained the directional charge flow in the HNV-4 heterostructure by site-specific platinum (Pt) photodeposition using the same light source that was used in the photocatalytic reduction of CO_2. The as-prepared samples are denoted as HNV-4@Pt. Together with Fig. S9†, the HR-TEM image of the HNV-4@Pt (Fig. 4e) shows the lattice fringes of ca. 3.36, 2.65, and 2.22 Å, matching well with the (111), (012), and (111) crystal facets of HCC, NiV-LDH, and Pt nanoparticles (NPs), respectively.[53] It can be observed that the Pt NPs tend to grow on the surface of HCC showing darker-colored black regions, and NiV-LDH exhibits small and thin nanosheets with light grey, suggesting that the photogenerated electrons tend to migrate to the surface of HCC for selective metal reduction. Generally speaking, the Pt NPs obtained by *in-situ* photodeposition are 5~10 nm in size with uniform dispersion. As shown in Fig. 4f, the HAADF-STEM and corresponding EDS mapping images clearly show that many clear and large-sized (ca. 15~20 nm) bright Pt spots are more centrally distributed on the surface of the sample. According to the microstructure characteristic, NiV-LDH in HNV-4 heterojunction uniformly covers the surface of HCC, resulting in a certain extent of masking of the active site on the HCC. As a result, a large number of photoelectrons accumulate on a small area of HCC and are then transferred to Pt^{4+}, promoting the reduction of Pt^{4+} and continued growth and aggregation of Pt NPs.[54] Assuming that Pt NPs are photo-deposited on the NiV-LDH, which is located in the outermost layer of the HNV-4 heterojunction, the size of the NPs should be relatively small and uniformly distributed. However, the above assumption is contrary to the experimental results in this work, which further validate that the photogenerated electrons of HNV-4 are mainly accumulated on HCC. In other words, in the HNV-4 heterojunction, the HCC acts as a reduction-type photocatalyst (RP) and NiV-LDH serves as an oxidation-type photocatalyst (OP).[55]

The interfacial charge separation and transfer efficiency of the HCC, NiV-LDH, and HNV-4 are tested by the photoelectrochemical measurement. As shown in Fig. 4g, the transient photocurrent response (TPR) intensity of the HNV-4 heterojunction is much higher than that of HCC and NiV-LDH, and the photo-response curve of HNV-4 appears the spike when the moment of the light source is turned on, owing to the instantaneous accumulation of light-induced charge carrier.[46] Moreover, the Nyquist plot of HNV-4 in the electrochemical impedance spectra (EIS) shows the smallest radius under the cover of darkness, suggesting the lowest resistance to inner electron transport between HCC and NiV-LDH (Fig. S10†). These results are consistent with TPR testing, further confirming that the successful construction of S-scheme heterojunction can effectively reduce the interfacial resistance of transferring photocarriers, which facilitates the carrier migration and modifies the electric field microenvironment of HNV heterojunction. According to the results of energy band structure, ESR test, photo-deposition Pt NPs sites, and photoelectrochemical measurement, an S-scheme electron migration pathway is proposed (Fig. 4h). Due to the Fermi level (E_f) of n-type semiconductors near the CB, the E_f of NiV-LDH is lower compared to that of HCC, and when NiV-LDH and HCC come into contact, the electrons inside HCC spontaneously migrate to NiV-LDH to reach an equilibrium of E_f. Note that, this fact is well following the results achieved in XPS under the ground state (Fig. 2a-e). At the same time, due to the enrichment of electrons on the surface of NiV-LDH, a built-in electric field (BIEF) from HCC to NiV-LDH is established, positively and negatively charged for HCC and NiV-LDH, respectively. With the presence of BIEF inducing the occurrence of band bending of the semiconductor, the photogenerated electrons on the CB (–0.30 V *vs*. NHE) of NiV-LDH can slide downwards along the bent energy band to the VB (0.57 V *vs*. NHE) of HCC and recombine with holes, thus

View Article Online
DOI: 10.1039/D4SC07856J

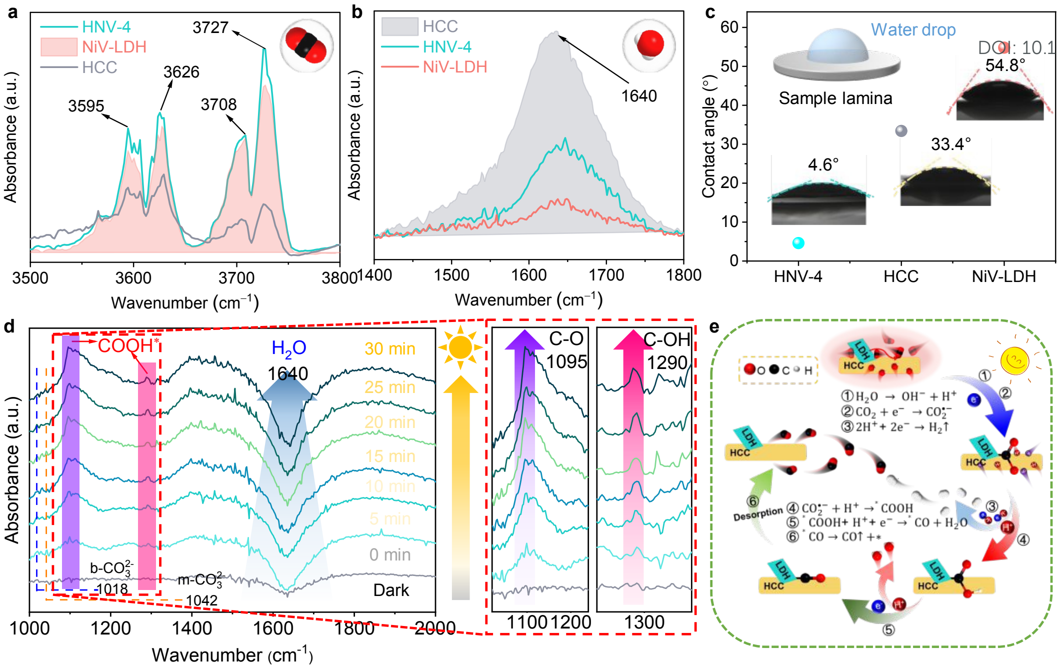

Fig. 5 (a) DRIFTS spectra of CO_2 adsorption for HCC, NiV-LDH, and HNV-4. (b) DRIFTS spectra of H_2O adsorption for HCC, NiV-LDH, and HNV-4. The insets are the corresponding molecular models of adsorption (upper right corner). (c) Water contact angles of HCC, NiV-LDH, and HNV-4. The inset is the corresponding experimental schematic (upper left corner). (d) *In-situ* DRIFTS spectra for the reaction of CO_2 with H_2O on HNV-4 under visible light ($\lambda > 420$ nm). (e) Proposed reaction mechanism based on the PCET process for photocatalytic green syngas synthesis over HNV heterojunction.

retaining a large amount of strong reducing electrons on HCC under the visible light irradiation.[56] The photogenerated electrons from the CB of the HCC (RP) reduce CO_2 and H_2O to syngas, and the photogenerated holes from the VB of the NiV-LDH (OP) are consumed by the sacrificial agent (TEOA). To sum up, the rational construction of the BIEF based on the S-scheme controllably modifies the electric field microenvironment of the HNV-4 heterojunction photocatalyst, which could promote the efficient separation of photoexcited charge carriers while maintaining its high redox capabilities. However, it is non-selective that the kinetic support provided for the reduction of CO_2 to CO associated with the proton-coupled electron transfer (PCET) reaction and the splitting of H_2O to H_2 through the proton (H^+) coupling process under the modulation of the electric field microenvironment alone.[24,57]

During the photoreduction of CO_2 with H_2O to produce syngas, the reaction microenvironment formed by the interaction between the surface of the photocatalyst and various molecules in the reaction system has an important influence both on the catalytic reaction rate and product selectivity.[58,59] Firstly, to investigate the actual adsorption state of reactant CO_2 molecules by the samples, we further characterize the as-prepared samples using diffuse reflectance infrared Fourier transform spectroscopy (DRIFTS).[60] The characteristic CO_2 absorption band with corresponding infrared peaks at 3595~3727 cm^{-1} can reflect the gas-phase CO_2 adsorption capability. As shown in Fig. 5a, the CO_2 adsorption ability follows the order of HNV-4 > NiV-LDH > HCC, indicating that the loading of NiV-LDH in the heterojunctions can facilitate CO_2 enrichment on the surface of the samples. The underlying reason is probably due to the intrinsic alkaline property of the LDH that makes it easier to capture acidic CO_2 molecules.[26] When NiV-LDH is assembled with HCC, the chemical interaction of HNV-4 with CO_2 is further enhanced due to the synergistic effect between the components, which favors the reduction of the chemically activated bond energies and reaction barriers of O=C=O. Compared with that of NiV-LDH, the DRIFTS spectrum for HCC shows the highest absorption peak at 1640 cm^{-1} (Fig. 5b), which is attributed to the vibration of adsorbed water molecules on the surface of the materials.[61] From the above results, the adsorption capability of the samples for CO_2 and H_2O molecules is in good agreement with the distribution of their catalytic reduction products, where both H_2 and CO are contained in the products of the HCC with high H_2 yields, and no H_2 is produced by the NiV-LDH, with the products containing only CO and trace CH_4. After introducing the NiV-LDH NSs, the absorption peak strength of H_2O molecular decreased for HNV-4 compared with the HCC, suggesting the NiV-LDH NSs could efficiently modulate the reaction microenvironmental of the HNV-4 heterojunction. Additionally, similar variations are exhibited in the water contact angle (WCA) results of Fig. 5c. The WCA from small to large is HNV-4 < HCC < NiV-LDH, and a smaller contact angle can adsorb more water molecules, which is favorable for H^+ production.[10]

The pathway of the reduction of CO_2 to CO over HNV-4 has been investigated by *in-situ* DRIFTS. Upon visible light irradiation, the absorption peaks at 1018 and 1042 cm^{-1} are assigned to the C-O stretching of the bidentate carbonate (b-CO_3^{2-}) and the monodentate carbonate (m-CO_3^{2-}) group, respectively, as a result of dissolved CO_2 in water (Fig. 5d).[21] The signals of the adsorbed carbonate species upon NiV-LDH are similar to that observed over NHV-4 and obvious as compared with the HCC (Fig. S11†). The vast alkaline hydroxyl group onto the LDH should be responsible for the favorable CO_2 adsorption process,[37] as reflected by the results in Fig. 5a. Noteworthy, the negative peak located at ca. 1640 cm^{-1} belongs to the H_2O molecules adsorbed on the surface of the sample, and the peak intensity increases gradually with the increase of the irradiation time, indicating that the water molecules adsorbed on the HNV-4 surface are continuously dissociated as the reaction proceeds. Then, CO_2 molecules adsorbed on the surface of the photocatalyst further react with H^+ produced by the dissociation of H_2O to produce *COOH intermediates. As shown in the localized zoomed-in image on the right side of Fig. 5d, *COOH is the most important intermediate produced by CO_2 activation, which gives rise to the peaks at 1095 and 1290 cm^{-1} (C-O and C-OH stretching, respectively) with the increased light irradiation time, proving that the photocatalytic CO_2 reduction process based on HNV-4 is consistent with Carbene pathway.[44]

For the CO_2 photocatalytic reduction reaction, the electron transfer is often accompanied by the simultaneous proton migration in the redox reaction, which is a PCET process. It is widely accepted that the PCET process is kinetically favored over electron transfer or proton transfer, and obtaining the H^+ by dissociating H_2O molecules, which is usually used as the H^+ source for CO_2 reduction in aprotic solvents.[8,35,62] As shown in Fig. 5e, based on the synergistic effect of the optimized electric field microenvironment and the reaction microenvironment, the photoreduction of CO_2 to green syngas processes over HNV heterojunction is as follows. A part of the H_2O molecules adsorbed on the surface of HCC and H^+ comes from the dissociation of H_2O molecules (Eq. 1). Meanwhile, NiV-LDH NSs capture CO_2 molecules from the surrounding reaction liquid and induce their enrichment in HNV heterojunction to form a high local concentration of CO_2. Then, the adsorbed CO_2 molecules are further activated to $CO_2^{\bullet-}$ (Eq. 2). A part of the H^+ is reduced by photogenerated electrons produced from the S-scheme HNV heterojunction after photoexcitation to form H_2 (Eq. 3). The activated $CO_2^{\bullet-}$ are further hydrogenated with the two-step PCET process to form the vital intermediate of *COOH and *CO (Eqs. 4 and 5).[63] Finally, the *CO desorption and spillover from the photocatalyst surface (Eq. 6). At this point, NiV-LDH NSs rationally modulate the microenvironment of the HNV heterojunction both of the electric field microenvironment and the reaction microenvironment. In detail, NiV-LDH NSs serve as the OP to accelerate the charge carriers separation based on the charge transfer pathway of the S-scheme, and while serving as the CO_2 collector to increase CO_2 concentration around the HCC (RP) active site. Based on the synergistic effect, the PCET process of the HNV-4 heterojunction is accelerated to promote the evolution of CO, simultaneously the production of H_2 is also modulated, resulting in high green syngas yield and an extended modulation of CO/H_2 ratio.

$$H_2O \rightarrow OH^- + H^+ \tag{1}$$

$$CO_2 + e^- \rightarrow CO_2^{\bullet-} \tag{2}$$

$$2H^+ + 2e^- \rightarrow H_2\uparrow \tag{3}$$

$$CO_2^{\bullet-} + H^+ \rightarrow {*}COOH \tag{4}$$

$${*}COOH + H^+ + e^- \rightarrow {*}CO + H_2O \tag{5}$$

$${*}CO \rightarrow CO\uparrow + {*} \tag{6}$$

4. Conclusions

In conclusion, a highly efficient CdS@NiV-LDH (HNV) photocatalyst is designed and fabricated *via* a simple oil bath method, in which the NiV-LDH NSs are uniformly grown *in-situ* on the surface of hollow cubic CdS. The HNV heterojunction photocatalyst presents a simple but highly effective analog of photosynthesizing plants, in which the NiV-LDH NSs mainly act as a CO_2 collector and light absorber and HCC offers the catalytic sites of both H_2O and CO_2. The electric field microenvironment is modified by redistributing space charge *via* a built-in electric field, while the adjusted reaction microenvironment promotes the local enrichment of CO_2 molecules, leading to the effective modulation of the PCET reaction process and facilitating the formation of *COOH intermediates over the prepared S-scheme heterojunction photocatalysts. As a result, the CO and H_2 evolution rates over the optimal HNV-4 heterojunction are 1163.8 μmol/g/h and 1334.6 μmol/g/h, respectively, with the optimized CO/H_2 ratio of 0.87 and the overall syngas formation rate of 2498.4 μmol/g/h. Moreover, adjustable CO/H_2 ratios ranging from 0.2 to 1 are obtained by adjusting the loading of NiV-LDH NSs. This work provides a distinctive insight into the modulation of the PCET reaction process through the rational design and optimization of the local microenvironment of heterojunction photocatalysts and achieves satisfactory CO_2 photoreduction activity and flexible regulation of green syngas ratio.

Author contributions

Senlin Zhang analyzed all data and drafted the manuscript. Yuheng Ma performed the experiments and gathered all the data. Changqiang Yu, Zhaohui Huang, and Ruoning Zhan help to check the manuscript. Yingxinjie Wang carried out water contact angle tests. Xiuqiang Xie and Nan Zhang co-guided this work and corrected the manuscript. All authors contributed to a critical discussion of the data and manuscript.

Conflicts of interest

There are no conflicts to declare.

Data availability

All data supporting the findings of this study are available within the paper and its ESI files.

Acknowledgements

This work was supported by the National Natural Science Foundation of China (52272295, 52071137, 51977071, 51802040, and 21802020), the Science and Technology Innovation Program of Hunan Province (2021RC3066 and 2021RC3067), and the Natural Science Foundation of Hunan

View Article Online
DOI: 10.1039/D4SC07856G

Province (2020JJ3004 and 2020JJ4192). N. Zhang and X. Xie also acknowledge the financial support of the Fundamental Research Funds for the Central Universities and the Shiyanjia Lab (www.shiyanjia.com) for providing XPS analysis, and thank the Analytical Instrumentation Center of Hunan University for SEM and HR-TEM characterizations.

References

1 P. F. Wang, Y. Li, N. R. Sun, S. B. Han, X. M Wang, Q. Q. Su, Y. J. Li, J. He, X. H. Yu, S. Y. Du, J. S. Francisco, J. L. Zhu and Y. S. Zhao, *Chem. Rev.*, 2024, **124**, 10363-10385.
2 Z. R. Xiao, H. Zhang, S. L. Zhang, X. Y. Tan, F. Ye, J. M Gu, J. J. Zou and D. S. Wang, *Fuel*, 2024, **362**, 130906.
3 F. Zhang, Z. Ma, Z. Shi, X. Chen, D. Wu, X. Li and C. Shan, *Energy Mater. Adv.*, 2021, **2021**, 5198145.
4 B. Chandran, J. K. Oh, S. W. Lee, D. Y. Um, S. U. Kim, V. Veeramuthu, J. S. Park, S. Han, C. R Lee and Y. H. Ra, *Nano-Micro Lett.*, 2024, **16**, 244.
5 N. Dewangan, W. M. Hui, S. Jayaprakash, A. R. Bawah, A. J. Poerjoto, T. Jie, A. Jangam, K. Hidajat and S. Kawi, *Catal. Today*, 2020, **356**, 490-513.
6 H. Zhang, Z. R. Xiao, P. Li, C. X. Zhang, X. Y. Tan, F. Ye, J. M. Gu, E. X. Yuan, J. J. Zou and D. S. Wang, *Sep. Purif. Technol.*, 2024, **350**, 127998.
7 S. W. Wang, J. S. Wang, Y. Wang, X. Y. Sui, S. H. Wu, W. X. Dai, Z. Z. Zhang, Z. X. Ding and J. L. Long, *ACS Catal.*, 2024, **14**, 10760-10788.
8 R. Paul, R. Das, N. Das, S. Chakraborty, C. W. Pao, Q. T. Trinh, G. T. K. K. Gunasooriya, J. Mondal and S. C. Peter, *Angew. Chem. Int. Ed.*, 2023, **62**, e202311304.
9 H. Z. Yang, D. R. Yang and X. Wang, *Angew. Chem. Int. Ed.*, 2020, **59**, 15527-15531.
10 C. F. Zhao, C. Yang, X. M. Lv, S. Y. Wang, C. J. Hu, G. F. Zheng and Q. Han, *Adv. Mater.*, 2024, **36**, 2401004.
11 B. Su, M. Zheng, W. Lin, X. F. Lu, D. Luan, S. Wang and X. W. (D.) Lou, *Adv. Energy Mater.*, 2023, **13**, 2203290.
12 H. Y. Wang, W. H. Xie, D. D. Wei, R. Hu, N. Wang, K. Chang, S. L. Lei, B. Wang and R. Cao, *ChemSusChem*, 2022, **15**, e202200200.
13 X. W. Lan, H. S. Li, Y. M. Liu, Y. Z. Zhang, T. J. Zhang and Y. Chen, *Angew. Chem. Int. Ed.*, 2024, **63**, e202407092.
14 A. Dey, J. Pradhan, S. Biswas, F. A. Rahimi, K. Biswas and T. K. Maji, *Angew. Chem. Int. Ed.*, 2024, **63**, e202315596.
15 P. Yadav, S. Kumar, N. Velankanni, T. D. Kühne, S. Gosavi, R. K. M. Raghupathy, R. Bhosale, G. Held, M. Shelke and S. Ogale, *J. Phys.: Energy*, 2024, **6**, 025019.
16 T. Tian, X. Y. Jin, N. Guo, H. Q. Li, Y. Han and Y. P. Yuan, *Appl. Catal., B*, 2022, **308**, 121227.
17 G. Z. S. Ling, V. B.-Y. Oh, C. Y. Haw, L.-L. Tan and W.-J. Ong, *Energy Mater. Adv.*, 2023, **4**, 0038.
18 P. Zhang, D. Y. Luan and X. W. (D.) Lou, *Adv. Mater.*, 2020, **32**, 2004561.
19 Y. Su, D. Ao, H. Liu and Y. Wang, *J. Mater. Chem. A*, 2017, **5**, 8680-8689.
20 P. Zhang, S. B. Wang, B. Y. Guan and X. W. (D.) Lou, *Energy Environ. Sci.*, 2019, **12**, 164-168.
21 Y. H. Ma, Y. Zhang, G. S. Xie, Z. H. Huang, L. F. Peng, C. Q. Yu, X. Q. Xie, S. L. Qu and N. Zhang, *ACS Catal.*, 2024, **14**, 1468-1479.
22 X. Yan, M. Yuan, Y. L. Yuan, P. Su, Q. Chen and F. X. Xiao, *Chem. Sci.*, 2024, **15**, 10625.
23 W. Huang, T. Bo, S. Zuo, Y. Wang, J. Chen, S. Ould-Chikh, Y. Li, W. Zhou and J. Zhang, *SusMat*, 2022, **2**, 466-475.
24 H. Cao, X. D. Zhu, J. W. Xue, R. Y. Wang, J. S. Shang, P. Y. Ma, C. Y. Liu and J. Bao, *ACS Catal.*, 2024, **14**, 9734-9741.
25 Q. L. Wang, X. W. Gao, Y. Wei, T. F. Liu, Q. K. Huang, D. Ren, S. M. Zakeeruddin, M. Grätzel, M. K. Wang, Q. Y. Li, J. J. Yang and Y. Shen, *ACS Appl. Mater. Interfaces*, 2024, **16**, 36462-36470.
26 C. J. Ning, S. Bai, J. K. Wang, Z. X. Li, Z. Y. Han, Y. F. Zhao, D. O'Hare and Y. F. Song, *Coord. Chem. Rev.*, 2023, **480**, 215008.
27 J. Li, G. Gao, Y. Liu, Y. Li and Z. Liu, *J. CO_2 Util.*, 2022, **65**, 102257.
28 S. Yu, L. Tan, S. Bai, C. J. Ning, G. H. Liu, H. J. Wang, B. Liu, Y. F. Zhao and Y. F. Song, *Small*, 2022, **18**, 2202334.
29 K. Teramura, S. Iguchi, Y. Mizuno, T. Shishido and T. Tanaka, *Angew. Chem. Int. Ed.*, 2012, **51**, 8008-8011.
30 J. Zhao, Y. Lu, D. B. Wu, Y. C. Qin, Y. Xie, Y. Guo, W. Raza, G. Luo, M. A. Mushtaq, Y. F. Wu, X. W. Mu, Y. Ling, T. Ilyas, Q. U. Hassan and C. M. Gao, *Sep. Purif. Technol.*, 2023, **305**, 122508.
31 A. Ziarati, A. Badiei, R. Grillo and T. Burgi, *ACS Appl. Mater. Interfaces*, 2019, **11**, 5903-5910.
32 T. Ishizuka and T. Kojima, *Acc. Chem. Res.*, 2024, **57**, 2437-2447.
33 Y. Z. Liu, A. X. Deng, Y. J. Q. Yin, J. K. Lin, Q. Li, Y. Sun, J. Q. Zhang, S. Y. Li, S. G. Yang, Y. Xu, H. He, S. M. Liu and S. B. Wang, *Appl. Catal. B-Environ. Energy*, 2025, **362**, 124724.
34 A. Li, H. Pang, P. Li, N. Zhang, G. Chen, X. G. Meng, M. Liu, X. H. Liu, R. Z. Ma and J. H. Ye, *Appl. Catal., B*, 2021, **288**, 119976.
35 M. H. Zhang, Y. Y. Mao, X. L. Bao, G. Y. Zhai, D. F. Xiao, D. Liu, P. Wang, H. F. Cheng, Y. Y. Liu, Z. K. Zheng, Y. Dai, Y. C. Fan, Z. Y. Wang and B. B. Huang, *Angew. Chem. Int. Ed.*, 2023, **62**, e202302919.
36 Y. B. Li, Z. L. Jin and N. Tsubaki, *J. Mater. Chem. C*, 2022, **10**, 18213-18225.
37 R. N. Wang, Z. Wang, Z. Y. Qiu, S. P. Wan, J. Ding and Q. Zhong, *Chem. Eng. J.*, 2022, **448**, 137338.
38 L. Tan, S. M. Xu, Z. L. Wang, Y. Q. Xu, X. Wang, X. J. Hao, S. Bai, C. J. Ning, Y. Wang, W. K. Zhang, Y. K. Jo, S. J. Hwang, X. Z. Cao, X. S. Zheng, H. Yan, Y. F. Zhao, H. H. Duan and Y. F. Song, *Angew. Chem. Int. Ed.*, 2019, **58**, 11860-11867.
39 Y. B. Li, Z. L. Jin and N. Tsubaki, *J. Mater. Chem. C*, 2022, **10**, 18213-18225.
40 K. Zeng, M. Chao, M. Tian, J. Yan, M. H. Rummeli, P. Strasser and R. Z. Yang, *Adv. Funct. Mater.*, 2024, **34**, 2308533.
41 A. Tyagi, M. C. Joshi, A. Shah, V. K. Thakur and R. K. Gupta, *ACS Omega*, 2019, **4**, 3257-3267.
42 E. González, J. Arbiol and V. F. Puntes, *Science*, 2011, **334**, 1377-1380.
43 H. C. Sun, H. C. Chen, M. Humayun, Y. Qiu, J. Ju, Y. M. Zhang, M. Bououdina, X. Y. Xue, Q. J. Liu, Y. J. Pang and C. D. Wang, *Adv. Funct. Mater.*, 2024, **34**, 2408872.
44 Y. O. Wang, E. Q. Chen and J. W. Tang, *ACS Catal.*, 2022, **12**, 7300-7316.
45 Y. Wang, G. Fan, S. Wang, Y. Li, Y. Guo, D. Luan, X. Gu and X. W. (D.) Lou, *Adv. Mater.*, 2022, **34**, 2204865.
46 H. Z. Liu, X. Liu, B. Li, H. Q. Luo, J. G. Ma and P. Cheng, *ACS Appl. Mater. Interfaces*, 2022, **14**, 28123-28132.
47 Q. L. Mo, J. L. Li, S. R. Xu, K. Wang, X. Z. Ge, Y. Xiao, G. Wu and F. X. Xiao, *Adv. Funct. Mater.*, 2023, **33**, 2210332.
48 L. Yang, L. Li, P. F. Xia, H. Y. Li, J. J. Yang, X. H. Li, X. D. Zeng, X. D. Zhang, C. Xiao and Y. Xie, *Chem. Commun.*, 2021, **57**, 11629-11632.
49 L. Tan, K. Peter, J. Ren, B. Y. Du, X. J. Hao, Y. F. Zhao and Y. F. Song, *Front. Chem. Sci. Eng.*, 2020, **15**, 99-108.
50 H. J. Wang, S. Bai, P. Zhao, L. Tan, C. J. Ning, G. H. Liu, J. K. Wang, T. Y. Shen, Y. F. Zhao and Y. F. Song, *Catal. Sci. Technol.*, 2021, **11**, 7091-7097.
51 Q. Meng, L. Wu, X. Yang, Y. Xiong, F. Kong and T. Duan, *SusMat*, 2024, **4**, e199.
52 Y. Yang, J. J. Wu, T. T. Xiao, Z. Tang, J. Y. Shen, H. J. Li, Y. Zhou and Z. G. Zou, *Appl. Catal., B*, 2019, **255**, 117771.

53 L. F. Peng, C. Q. Yu, Y. H. Ma, G. S. Xie, X. Q. Xie, Z. J. Wu and Nan Zhang, *Inorg. Chem. Front.*, 2022, **9**, 994-1005.
54 N. F. Wang, S. Cheong, D. E. Yoon, P. Lu, H. Lee, Y. K. Lee, Y. S. Park and D. C. Lee, *J. Am. Chem. Soc.*, 2022, **144**, 16974-16983.
55 L. Zhang, J. Zhang, H. Yu and J. Yu, *Adv. Mater.*, 2022, **34**, 2107668.
56 J. H. Hua, C. C. Ma, D. Y. Wu, H. T. Huang, X. J. Dai, K. D. Wu, H. H. Wang, Z. W. Bian and S. Feng, *J. Alloys Compd.*, 2024, **970**, 172516.
57 P. Hutchison, A. V. Soudackov and S. H. Schiffer, *ACS Catal.*, 2024, **14**, 14363-14372.
58 Z. Y. Xu, X. Tan, C. Chen, X. D. Wang, R. Sui, Z. B. Zhuang, C. Zhang and C. Chen, *Natl. Sci. Rev.*, 2024, **11**, nwae315.
59 T. Baran, M. Aresta, R. Comparelli and A. Dibenedetto, *ChemSusChem*, 2024, **17**, e202400661.
60 L. Cheng, X. Y. Yue, L. X. Wang, D. N. Zhang, P. Zhang, J. J. Fan and Q. J. Xiang, *Adv. Mater.*, 2021, **33**, 2105135.
61 P. L. Sun, X. X. Cheng, Y. H. Lai, Z. Q. Wang, C. Y. Ma and J. C. Chang, *RSC Adv.*, 2018, **8**, 36604-36615.
62 X. Z. Wang, S. L. Meng, J. Y. Chen, H. X. Wang, Y. Wang, S. Zhou, X. B. Li, R. Z. Liao, C. H. Tung and L. Z. Wu, *Angew. Chem. Int. Ed.*, 2021, **60**, 26072-26079.
63 B. Su, Y. Kong, S. Wang, S. Zuo, W. Lin, Y. Fang, Y. Hou, G. Zhang, H. Zhang and X. Wang, *J. Am. Chem. Soc.*, 2023, **145**, 27415-27423.

View Article Online
DOI: 10.1039/D4SC07856J

View Article Online
DOI: 10.1039/D4SC07856J

Data Availability Statement

All data supporting the findings of this study are available within the paper and its ESI files.